Research Square

Preprints are preliminary reports that have not undergone peer review.
They should not be considered conclusive, used to inform clinical practice,
or referenced by the media as validated information.

A universal microscope add-on for snapshot quantitative phase imaging by spectral encoding

Jinli Suo

jlsuo@tsinghua.edu.cn

Tsinghua University https://orcid.org/0000-0002-3426-1634

Weihang Zhang

Tsinghua University https://orcid.org/0000-0003-3717-9473

Xin Liu

Tsinghua University

Wenxuan Miao

Tsinghua University

Hai Qi

Tsinghua University

Qionghai Dai

Tsinghua University https://orcid.org/0000-0001-7043-3061

Article

Keywords:

Posted Date: June 4th, 2024

DOI: https://doi.org/10.21203/rs.3.rs-4420203/v1

License: This work is licensed under a Creative Commons Attribution 4.0 International License.
Read Full License

Additional Declarations: (Not answered)

A universal microscope add-on for snapshot quantitative phase imaging by spectral encoding

Weihang Zhang[1,†], **Jinli Suo**[1,2,6,†,*], **Xin Liu**[3,4,5,7,†], **Wenxuan Miao**[3,4,5,7], **Hai Qi**[3,4,5,7,*], **and Qionghai Dai**[1,2,*]

[1]Department of Automation, Tsinghua University, Beijing 100084, China
[2]Institute for Brain and Cognitive Sciences, Tsinghua University, Beijing 100084, China
[3]Laboratory of Dynamic Immunobiology, Institute for Immunology, Tsinghua University, Beijing 100084, China
[4]Department of Basic Medical Sciences, School of Medicine, Tsinghua University, Beijing 100084, China
[5]Tsinghua-Peking Center for Life Sciences, Beijing 100084, China
[6]Shanghai Artificial Intelligence Laboratory, Shanghai 200232, China
[7]Changping Laboratory, Beijing 100084, China
[*]jlsuo@tsinghua.edu.cn; qihai@tsinghua.edu.cn; qhdai@tsinghua.edu.cn
[†]These authors contributed equally to this work

ABSTRACT

Observing the dynamics of colorless or transparent samples quantitatively is vital in cellular-level biomedical research. Among existing techniques, fluorescent microscopy suffers from phototoxicity and photobleaching issues, while snapshot quantitative phase imaging (QPI) demands a complicated setup. Thus, an easily accessible tool allowing for long-period, high-contrast observation of transparent samples remains still lacking. To tackle this problem, we propose a one-shot QPI approach compatible with both off-the-shelf and customized microscopes, which encodes the phase informative cues into a snapshot using a thin, flat optical device and decodes the phase information through an advanced deep network algorithm. The encoding involves overlaying defocused images obtained through a wafer-thin highly-dispersive glass with dual-bandpass coating, acting as an "add-on" module located between the specimen and objective. The successive phase retrieval is conducted with a well-designed network structure and the high-quality training data supports the phase reconstruction at high axial resolution. By experimenting on T cell migration, T cell activation, and real-time live-cell drug screening on systems with various magnifications, we demonstrate high-precision phase retrieval of our method under different experimental settings and on various platforms, which is expected to obtain a wide range of potential applications in studies of clustered cell morphology, cell counting, and cell migration tracking.

1 Introduction

Dynamic microscopy of cells or tissues in their native state is pivotal to biological research, but most biological samples are transparent and cannot be observed directly. Fluorescence microscopy enables observing such transparent structures with high contrast by labeling specific molecules but brings along phototoxicity and photobleaching which harms the live specimen and thus hinders long-period observation. To address this issue, phase imaging has emerged as developing label-free techniques, using the phase change produced as light travels through materials with varying refractive indexes[1]. Different from traditional sensors can only measure the intensity of incoming light, phase imaging aims to profile the sample with quantitative information such as dry mass[2–4] but lessened damage, by deriving the refractive index or the phase distribution of the target sample from its plain intensity[5]. After decades of development, various implementations have been designed, including qualitative methods such as Zernike phase contrast microscopy[6,7], differential interference contrast microscopy[8], as well as quantitative phase imaging (QPI)[9]. These phase imaging techniques have found broad use in investigating the behaviors of neurons[10,11], fibroblasts[12], immune cells[13], cancer cells[14,15], chondrocytes[16], bacteria[17,18] and tissues[19–21].

QPI has garnered widespread interest for its ability to precisely depict changes in the local refractive index. At present, QPI methods can be mainly divided into categories using either interferometric[3,22] or non-interferometric [23,24] systems respectively[25,26]. In the former category, a common approach is to use an interferometer to generate the interference pattern of the sample beam and the reference beam, allowing for the extraction of the phase shift in the sample beam[27,28]. However, the interference setup faces challenges like complexity, sensitivity to vibration[29], and limited resolution[30]. Inspired by the principle of interferometry, the digital holography formed with coherent illumination offers phase estimation[31–35] by directly analyzing the acquired holographic patterns without mechanical scanning of interference fringes[36], but is slow

for capturing fast dynamics. One can accelerate acquisition using a programmable spatial light modulator (SLM) such as LCoS[37,38] or digital micromirror arrays (DMDs)[39] albeit at the expense of setting up a complex system, or embedding multiple holograms into a single acquisition[40,41] using an expensive and expertise-demanding temporally coherent light source and engaging in phase retrieval with a deep neural network[20]. To retrieve phase from a single intensity image, controlled illumination is also adopted for phase encoding[42]. The resolution loss caused by holographic reconstruction is another challenge faced by digital holography[43], which often necessitates the use of additional high-resolution objective lenses for compensation[44].

To overcome the common limitations of the complex and sensitive double-path systems used in interferometric QPI, a key strategy in non-interferometric QPI involves taking multiple acquisitions with varying off-axis distances[5,45] or illumination angles[46–49]. However, this approach still encounters constraints in frame rate, especially for capturing dynamic activities in live samples. One prevalent method in this domain is solving the Transport of Intensity Equation (TIE)[50,51] with the axial intensity differential derived from a focal stack captured at different axial positions[52], in different channels[53]. This can be carried out across various channels[53], with asymmetric[24,54,55] or epi-mode illuminations[56]. As an iterative method, Fourier ptychography conducts phase retrieval from images with different acquisition angles[57,58]. For faster observation, improved methods focus on reducing the number of acquisitions to achieve efficient phase retrieval. These methods include encoding the required measurements using multiple sensors[59,60], capturing data in a snapshot such as an RGB image[61], a light field[62], two regions of the sensor[63,64], or at least three modulated images[65]. By using a microlens array to collect the wavefront changes induced by phase shift[66,67], wavefront sensing retrieves the phase through numerical reconstruction[68] from a snapshot input[69], but with moderate spatial resolution[70], thus is only suitable for samples with nearly uniform intensity and smooth phase[71]. Alternative methods involve embedding phase data using the deformation of structured illumination[72] or a binary mask[73]. The lightweight QPI systems are further proposed by integrating the developing metasurface[74,75]. While the mentioned techniques require specialized optical engineering knowledge, a more straightforward approach suitable for both off-the-shelf and customized microscopes is more favorable.

In addition to constructing special configurations for phase encoding and decoding, recent studies have tapped into the impressive representation capability of deep neural networks to fit the phase object and the light propagation toward the measured intensity[76–78]. Such a paradigm negates the necessity for specialized setups in phase imaging but demands extensive tailoring of the network for the specific phase object, hindering real-time inference. The slow inference is a notable downside in practical scenarios, prompting a demand for a single-shot QPI method that offers improved efficiency.

In this article, we propose to design a scheme capable of encoding phase cues into a single snapshot, allowing for real-time phase retrieval in various microscopes. The workflow is depicted in Fig. 1(a). In terms of encoding, we introduce a thin flat optical glass of sub-millimeter thickness, compatible with a range of microscopes, either commercial or customized ones. For decoding, we design and train a deep neural network with superb performance. We incorporate the proposed design into microscopes of different sizes and magnifications to observe live cell behaviors in diverse settings, such as T cell migration and activation, live-cell drug screening, etc. The ability to observe live cells non-invasively for extended periods with high axial resolution across different platforms highlights the substantial advantages of this proposed method over traditional brightfield and fluorescence imaging techniques.

2 Results

The encoding and decoding scheme

Studies tell that one can derive the quantitative phase from a pair of defocused images captured at two opposite defocus distances[79]. Drawing inspiration from this principle, we propose to superimpose these two intensity images revealing phase information into a snapshot and design a deep neural network to decode the phase distributions, as illustrated in Fig. 1(a). For easy implementation, we utilize the property that defocus is wavelength dependent, and propose to use a dual-bandpass illumination filtered from a brightfield light source together with a highly-dispersive element shown in the orange box in Fig. 1(b) to generate two different defocused images and superimpose them onto the sensor.

Taking the working mode of an inverted microscope shown in Fig. 1(b) for illustration, the scheme of our setup is shown in Fig. 1(c). Specifically, we first introduce a dual-bandpass filter between the sample and the objective lens to modulate the brightfield illumination, with a customized spectral profile shown in Fig. 1(d). However, due to the achromatic design of modern microscopes, the intensity images corresponding to two composite narrow bands are similar. To magnify the difference, we adopt the glass sheet with a low Abbe coefficient (Schott, N-SF66) as the substrate of the dual-bandpass coating before the light enters the achromatic system, with the light path sketched in Fig. 1(e). With a proper thickness and location, the customized flat glass sheet can map the intensity images at opposite sides of the focal plane onto the sensor. By vertically adjusting the sample stage to locate the specimen between focal planes corresponding to two narrow band wavelengths, the defocused intensity images at two distinct axial positions are superimposed on the sensor and result in an image with fringes informative for phase as exampled in Fig. 1(a) and the upper block in Fig. 1(f). Benefiting from the single snapshot acquisition scheme, the proposed method can be applied to observe the behaviors of living cells at various speeds and depict their deformation and displacement for further analysis. Besides, the proposed scheme introduces only a wafer-thin element that can be easily manufactured at low

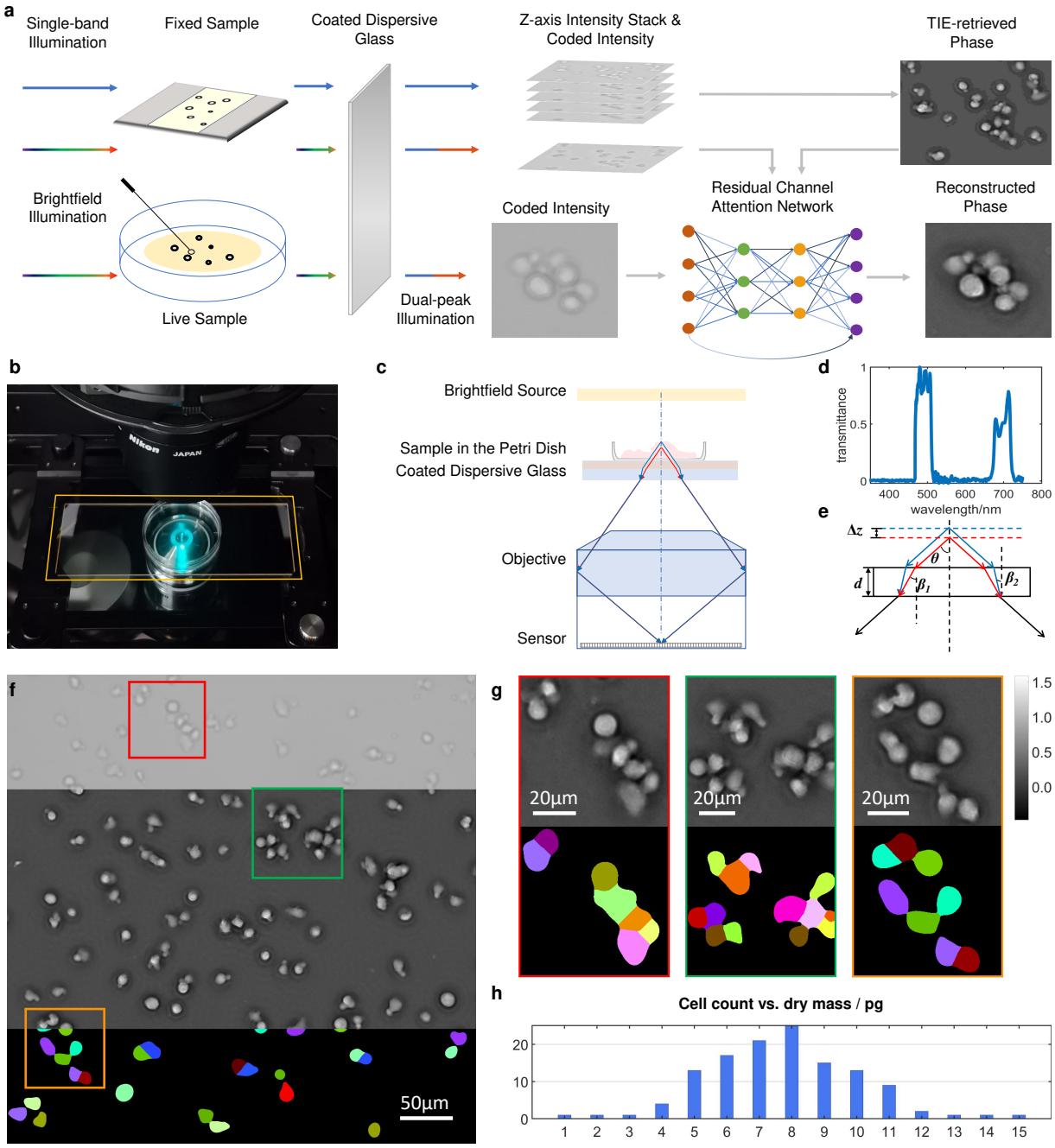


Figure 1. The schematic of the experimental setup and pipeline. (a) The workflow of the proposed scheme. The upper path shows the training steps of the phase retrieval network, in which fixed cells are used to capture the network input under dual-bandpass illumination and derive the ground-truth phase from the z-axis stack acquired under single-bandpass illumination. The lower steps depict the pipeline of live cell experiments, in which the dual-bandpass illumination is applied to generate a encoded intensity image serving as the network input for phase inference. (b) The experimental setup implemented on a Nikon Ti inverted microscope, where the "add-on" component in the orange box is located between the objective lens and the sample, fabricated by applying a customized dual-bandpass coating on a highly-dispersive flat glass sheet. (c) The schematic diagram of the proposed "add-on", in which the images at both sides of the focal plane are propagated by the two narrow wavebands respectively and superimposed onto the sensor. (d) The transmittance curve of the customized spectral coating. (e) The zoomed-in light path for obtaining the encoded measurement. (f) A representative phase reconstruction result, with the upper, middle, and bottom blocks demonstrating the encoded intensity measurement, reconstructed phase, and the cell segmentation map derived from the phase distribution. Here different colors represent different cells. (g) Three regions of interest in (f) and the corresponding segmentation results. (h) Dry mass histogram derived from the segmented phase map.

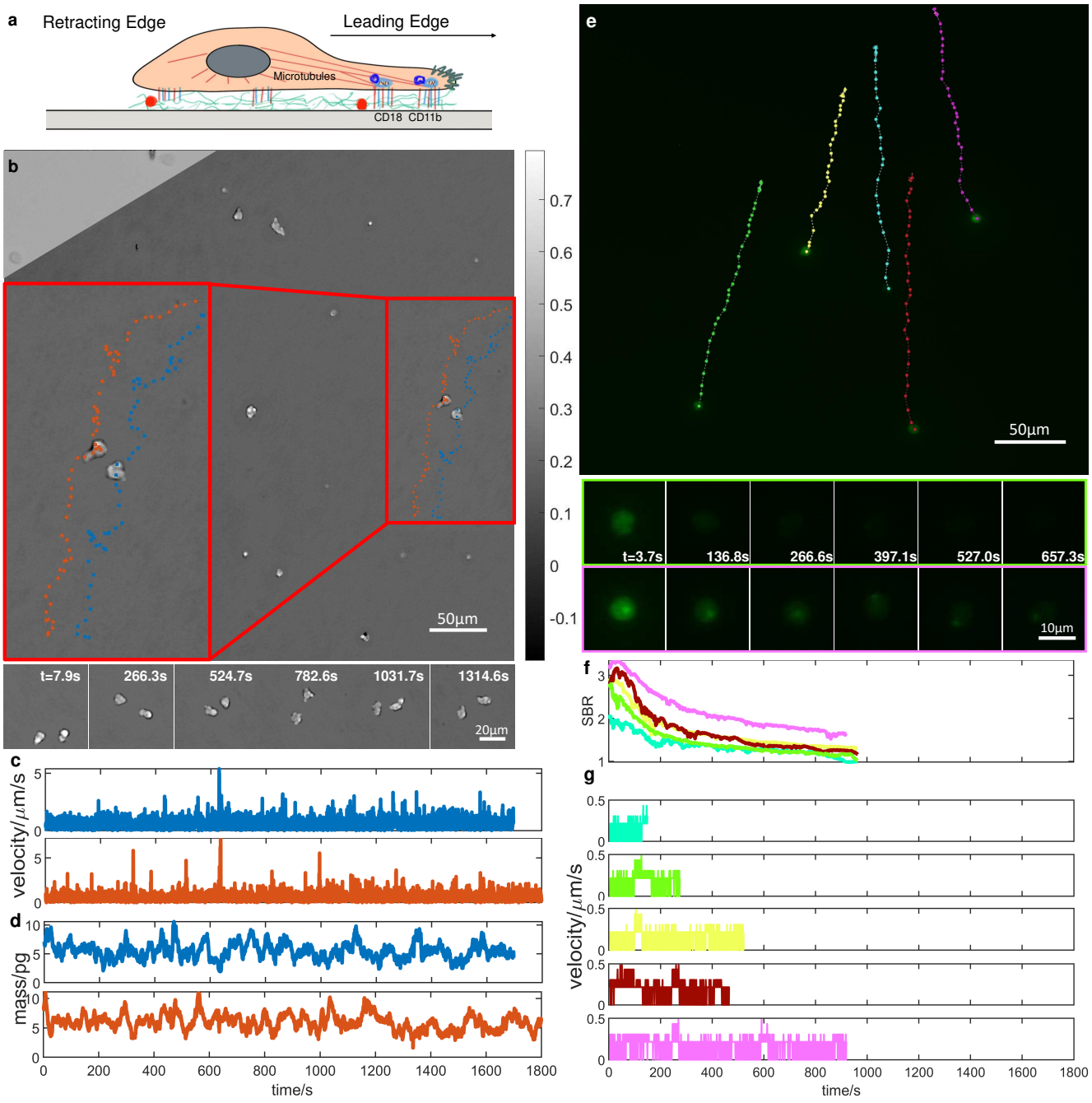


Figure 2. Comparison of the quantitative phase reconstruction and fluorescence imaging in the time-lapse acquisition of the migration of T cells mediated by integrin LFA-1. The QPI is conducted for 30 mins with the brightfield module, and the fluorescence images are conducted for 16 mins. The exposure time is 800ms per frame. (a) The schematic plot of the T cell migration process. (b) Encoded intensity image (upper left) and phase image (lower right) of the field of view captured at 13.8 mins. The orange and blue curves track the centroid movement of two representative cells respectively. The lower images are the zoomed-in phase sequences of the region of interest, which tracks the location of two cells. (c) The temporal traces of the lateral velocity of the two cells, derived from the movement of phase centroids. (d) The temporal traces of the dry mass change in the cell migration deduced from the phase distribution. (e) The fluorescence image of five representative cells captured at 3.7s. The curves in different colors indicate their migration traces. The lower images are the zoomed-in time-lapse sequences of two cells with green and purple traces respectively. (f) The temporal traces of the signal-to-background ratio (SBR) depicted by the ratio of average intensity of the segmented cells and their adjacent background. (g) The temporal traces of the velocities of the five cells derived from the movement of the cell region centroids.

cost to encode the illumination and generate dispersion, and thus is fully compatible with various microscopes and serves as a non-invasive high-contrast imaging mode working in an "add-on" manner.

Although the fringes are phase-informative, it is nontrivial to retrieve the phase analytically. Here we resort to supervised deep learning for high-quality phase retrieval. By using the proposed setup, a well-aligned defocused image stack can be captured by simply replacing the dual-bandpass filter after the brightfield source with a single-bandpass one, as shown in the upper path in Fig. 1(a), and the system is shown in Supplementary Fig. 2. Afterward, we employ a phase-deriving algorithm[79] based on the Transport of Intensity Equation[50] to obtain the ground-truth phase (see Methods) for supervised learning of the phase retrieval network. The network follows a residual channel attention architecture[80], as shown in Supplementary Fig. 1. After ∼100 hours training, the reconstructed phase distribution accurately depicts the cell shape and height, as shown in the middle block in Fig. 1(f) and the zoomed-in regions in Fig. 1(g). The quantitative analysis of the axial accuracy is provided in Supplementary Fig. 3, demonstrating the performance of the adopted network.

Benefiting from the high contrast and precision provided by the reconstructed phase, the QPI results can be readily used in cell segmentation, dynamic tracking, and dry mass calculation[81]. We performed cell segmentation with CellPofiler[82] and ilastik[83], with the results shown in the lower block in Fig. 1(f) and the zoomed-in regions in Fig. 1(g). Afterward, the dry mass distribution of the FOV in Fig. 1(f) is calculated by the concept of dry mass surface density[81] (see Methods) and shown in Fig. 1(h).

Long-term live-cell QPI with low photobleaching

Cell migration is one of the basic cellular physiological responses playing an important role in the immune system, among which cytotoxic T cells are important components of the adaptive immune system, capable of killing viral infected or abnormal cells. To fulfill their function, T cells need to migrate through complex tissue environments and be recruited to the site rapidly[84], as shown in Fig. 2(a). A better understanding of their migratory behaviors is essential to the development of strategies for the modulation of their effector function. The migration process often undergoes a long period and thus long-term observation is highly desired, however, such observation is hampered in fluorescent microscopy due to phototoxicity and photobleaching. To demonstrate the advantage of our single-shot QPI for long-term dynamic observation, we compare our imaging results against the wild-type GFP fluorescent microscopy in observing the migration of T cells mediated by integrin LFA-1, which interacts with its ligand ICAM-1 coated on glass slides, under a Nikon ECLIPSE Ti2-E microscope with 20× magnification. The details of cell preparation are described in Methods.

In fluorescence imaging, we track the migration of five cells shown in Fig. 2(e), where the zoomed-in images of two representatives at various time points are also displayed, demonstrating that the shape of cells gradually become blurry and the luminance becomes dark due to severe photobleaching. According to Fig. 2(f), during the 16-minute imaging process, the fluorescence intensity gradually weakens and leads to the attenuated signal-to-background ratio (SBR), thus challenging the accuracy of cell tracking. As shown in Fig. 2(g), the velocity tracking algorithm fails after a short period due to the severely weakened and buried signal. On the contrary, the phase map by the proposed approach remains stable in the long-term exposure as shown in the lower right column of Fig. 2(b), which is reconstructed from the brightfield encoded image shown in the left column captured at 13.8min, and the orange and blue curves track the centroid movement of the two representative cells respectively. Moreover, the cell contour and the sub-cellular phase fluctuations are observed in the trajectories in the zoomed-in sequences, which demonstrates that the proposed QPI method exhibits low photobleaching and phototoxicity, and thus achieves performance beyond conventional fluorescence imaging. The continuous cell migration details could be further observed in Supplementary Video 1.

The cell migration is achieved by the motion of the pseudopodia protrusion, which could also be truthfully recorded as cell deformation in the reconstructed phase distribution. Furthermore, by conducting cell segmentation in the phase sequences and deriving the coordinates of the cell centroid from the phase distribution, the velocity in Fig. 2(c) and dry mass changes in Fig. 2(d) in the cell migration process are easily inferred from the centroid displacement and phase value respectively, providing more potential for further quantitative exploitations.

Fine-scale morphological deformation analysis from high fidelity QPI

We further explore the unique ability of the proposed approach to retrieve subcellular morphological deformation from high-axial-resolution phase reconstruction. Specifically, we implement our setup for the visualization of the T cell activation process. Upon antigen recognition, T cells forge dynamic close contacts with the target cells, which help direct the cytotoxic factors and prevent bystander killing[85]. To mimic this process, we coated the imaging surface with both ICAM-1 and the anti-CD3 antibodies to activate the T cell receptor, as shown in Fig. 3(a). In the activation process, the cell morphology is subtle and almost visible in brightfield microscopy. Due to its close relation to axial deformation, cell morphology can be inferred from the quantitative phase distribution. Here we capture the cell dynamics with our setup and analyze the axial profiles at high accuracy.

Two representative cells are tracked, as shown in the upper rows in Fig. 3(b) and (c), where the intensity images only depict limited contour information with low contrast. On the contrary, the reconstruction results of the proposed QPI network exhibit high contrast and rich sub-cellular details. As shown in the lower rows in Fig. 3(b)(c) and Supplementary

Video 2, the cell deformation in the frames after the adhesion happens can be observed at 9.12s and 64.40s respectively. Further, it is quantitatively characterized by the temporal sequences of phase profile in Fig. 3(d), where the adhesion is manifested in the decreasing height in Fig. 3(d), indicated by the blue and orange arrows. Moreover, the universal coordinate system witnesses the detailed lateral movement of the two cells during the long-term observation. The motion characteristics of cells can also be highlighted by the evolution of the $x-y$ plane cross-sectional area in Fig. 3(e). Specifically, the slight enlarging of the cross-section in Fig. 3(e), and the blurring of the boundary (i.e., the pseudopodia protrusion) indicated by the red arrows in Fig. 3(c) can be observed. Furthermore, the dry mass change in the cell adhesion process is quantitatively deduced from the phase distribution as shown in Fig. 3(f), which has the potential to guide the study of transient particle transport in T cell activation. The training data used in this phase reconstruction model are from the z-axis stacks of 10 different FOVs acquired in advance on a fixed group of the same batch of cells. The complete time-lapse QPI result of the two cells is shown in Supplementary Video 2.

High throughput drug screening at different magnifications and various setups

Besides maintaining their stable state when observing the deformation of single cells with high contrast for a long period, the proposed QPI method is also proven to be capable of achieving time-lapse imaging of dense cells at various experimental setups, showing significant potential in high-throughput drug screening. Since a dispersive element is introduced between the objective lens and the sample, one may be concerned whether its existence might disturb the imaging of some systems, especially at high magnifications, which may hinder the applications of the proposed method. To clear such doubt, besides the above experiments on the common coverglass bottom dishes, we further prove the simplicity and versatility of the proposed method by conducting miniaturized screening experiments with three different cell culture plates using objective lenses with matching magnifications. Here five compounds that have been scientifically proven to be related to integrins are selected and injected into different wells of cell culture plates at specific concentrations: A-286982 (CAS No.: 280749-17-9), BIRT 377 (213211-10-0) BMS-688521 (893397-44-9), Leukadherin-1 (344897-95-6) and Lifitegrast (1025967-78-5).

The input and reconstructed phase of the cells in the first setup are shown in Supplementary Video 3, and a local and a global representative snapshot are displayed in Fig. 4(a) and Supplementary Fig. 4 respectively. The cell migration under the effect of compounds is observed by scanning among eight wells of Nunc™ Lab-Tek™ II Chambered Coverglass Thermo Scientific™ with 10× magnification. The cells in the first well serve as the control group where the same amount of PBS is added. The compound concentrations in the other wells are set near the half maximal inhibitory concentration (IC50) described in the MCE Library (www.medchemexpress.com). For Leukadherin-1, it is set according to the concentration for 50% of maximal effect (EC50). With the aid of the trained channel attention network, only a single snapshot of each well in every round of scanning is needed for calculating the real-time phase map. Afterward, the average velocity of cells is calculated by segmenting the reconstructed phase images and retaining the cell traces with a duration longer than 15 frames. As a result, the velocity vector diagram corresponding to the upper local snapshot and the violin diagram of cell velocities in eight wells are shown in the middle and lower rows of Fig. 4(a), which demonstrates the significant effect for promoting cell migration of Leukadherin-1 and the inhibition in other wells. For the two compounds that two different concentrations are applied, the enhanced antagonism produced by the high concentration can also be observed.

In the second and third experiments, 48-well and 384-well cell culture plates are used under 20× and 25× objectives respectively, and each compound is set with three or four concentration gradients. The results of these two experiments are shown in Supplementary Figs. 5 and 6, and the derived velocity plots are shown in Fig. 4(b) and (c) respectively, revealing the distinguished effect of different compounds. Especially, the 48-well experiment is conducted with an Olympus IXplore Live Microscope, while the other experiments in this paper are with Nikon ECLIPSE Ti2-E. Despite the shorter working distance at high magnification, we just need to reduce the thickness of the dispersive element from 1mm to 0.5mm.

By successive analysis of the high-throughput phase output, the QPI pipeline also verifies the effect of several compounds that modulate integrin activation and T cell migration, including the small molecule inhibitors for ICAM-1 and LFA-1 interactions, such as A-286982, BIRT 377, BMS-688521 and Lifitegrast, as well as Leukadherin-1, an agonist for MAC-1. In conclusion, the proposed QPI workflow performs stably under different experimental conditions and provides a plug-and-play high-throughput QPI solution.

3 Discussion

We propose a single-shot quantitative phase imaging approach by inserting a specially designed flat optical element into an off-the-shelf or customized brightfield microscope to encode the phase information and build an end-to-end deep neural network for algorithmic decoding. Besides the profit of long-term observation for all the label-free microscopy techniques, the proposed approach is advantageous in the following aspects:

i We can reconstruct a highly accurate phase due to elegant information encoding, high-quality training data acquisition, and a well-designed network structure.

ii As a single-shot approach, our approach can be applied to live cell observations at the same frame rates as brightfield microscopy by simply increasing the illumination intensity to compensate for the attenuation by dual-bandpass filter.

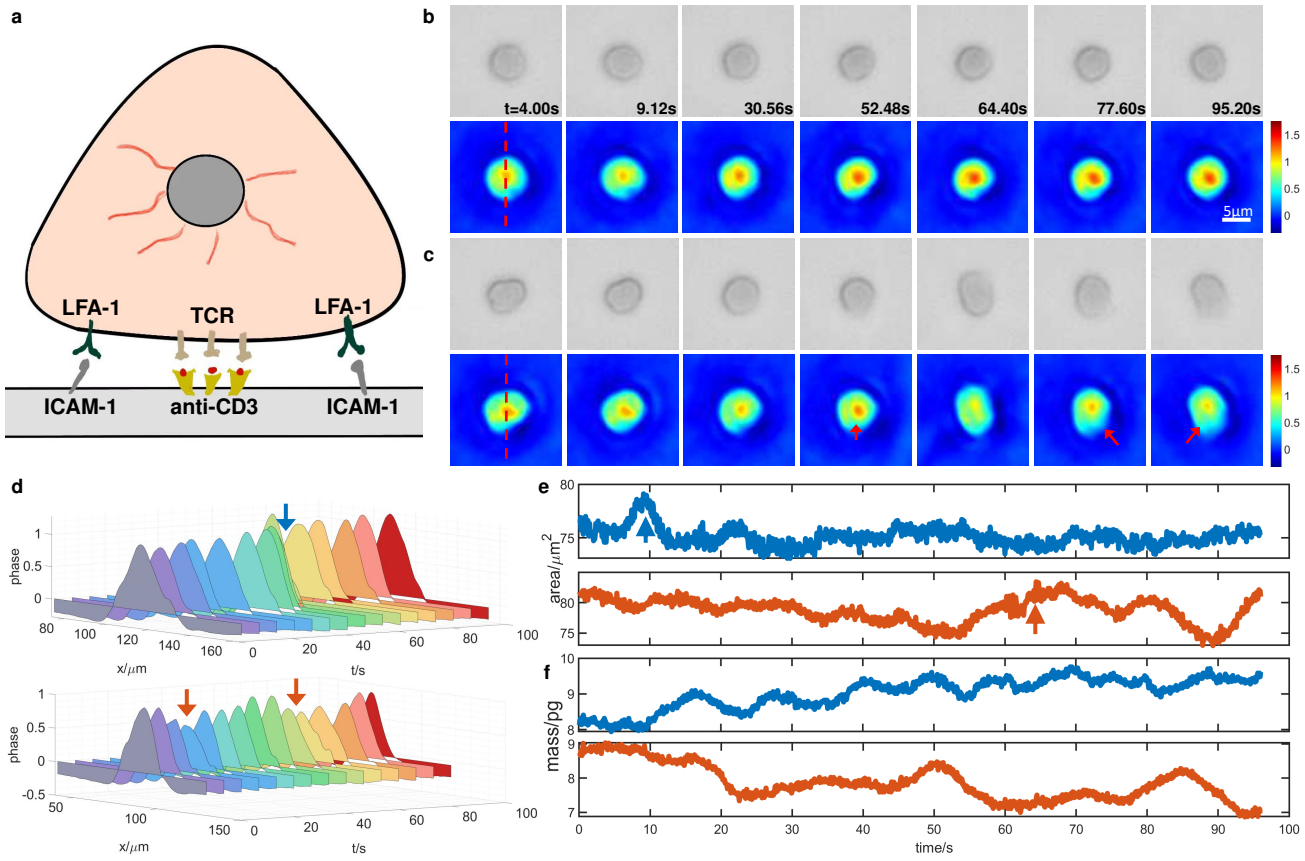


Figure 3. Quantitative phase reconstruction of the T cell activation process. (a) The schematic plot of the T cell activation process. (b, c) The encoded intensity (upper) and the phase (lower) sequences of two representative cells selected from the encoded videos captured with an exposure time of 80ms. The blurring of the boundary brought by the pseudopodia protrusion is indicated by the red arrows. (d) Temporal sequences of phase profile of the selected cells at 15 different timestamps. The profiles are acquired from the red dashed lines in (b) and (c). (e) The temporal traces of the cross-sectional area of the two cells. The slight enlarging of the cross-section, which possibly depicts the adhesion, is indicated by the blue and orange arrows at 9.12s and 64.40s respectively. (f) The temporal traces of the dry mass change in the cell adhesion process deduced from the phase distribution.

iii The scheme uses only a thin flat glass sheet and a partially coherent light source, and thus is fully compatible with both commercial and self-built microscopes, serving as a non-invasive high-contrast observation "add-on".

iv The training data can be easily derived from fixed samples captured from the same setup by adding a single narrow-band filter, and can be adapted to new cells at low cost.

Benefiting from these virtues, the approach facilitates non-invasive and high-quality observation of biomedical dynamics in their native state. We demonstrate the applications of observing cell behaviors, including T cell migration imaging at a similar frame rate to brightfield microscopy, and high-throughput cell population imaging at various experimental setups. Equipped with such a compatible setup and high-performance reconstruction, our approach can potentially become a standard imaging mode for on-hand microscopes.

Similar to other learning-based methods, our approach also has some limitations. On the one hand, we build cell-specific reconstruction networks for good performance. A general network applied for varying cell types is a better option, so a network being able to extract the phase information is a worth studying topic, which might inspire new network design and training strategies such as meta-learning. The recent rapid progress in big models might provide some valuable insights into both network design and effective training. On the other hand, the required large-scale training data results in a time-consuming training procedure. One can adopt a sampling strategy reducing the size of the training data set while covering the cell diversity simultaneously and design a low-weight network structure to shorten the training time.

In addition, although the proposed approach is highly compatible with different microscopes and across various settings, when objectives with higher magnification are involved the manufacturing of thinner dispersive substrate may pose a challenge. At present, we have been exploring approaches to directly adhere the glass to the bottom of the Petri dish or even

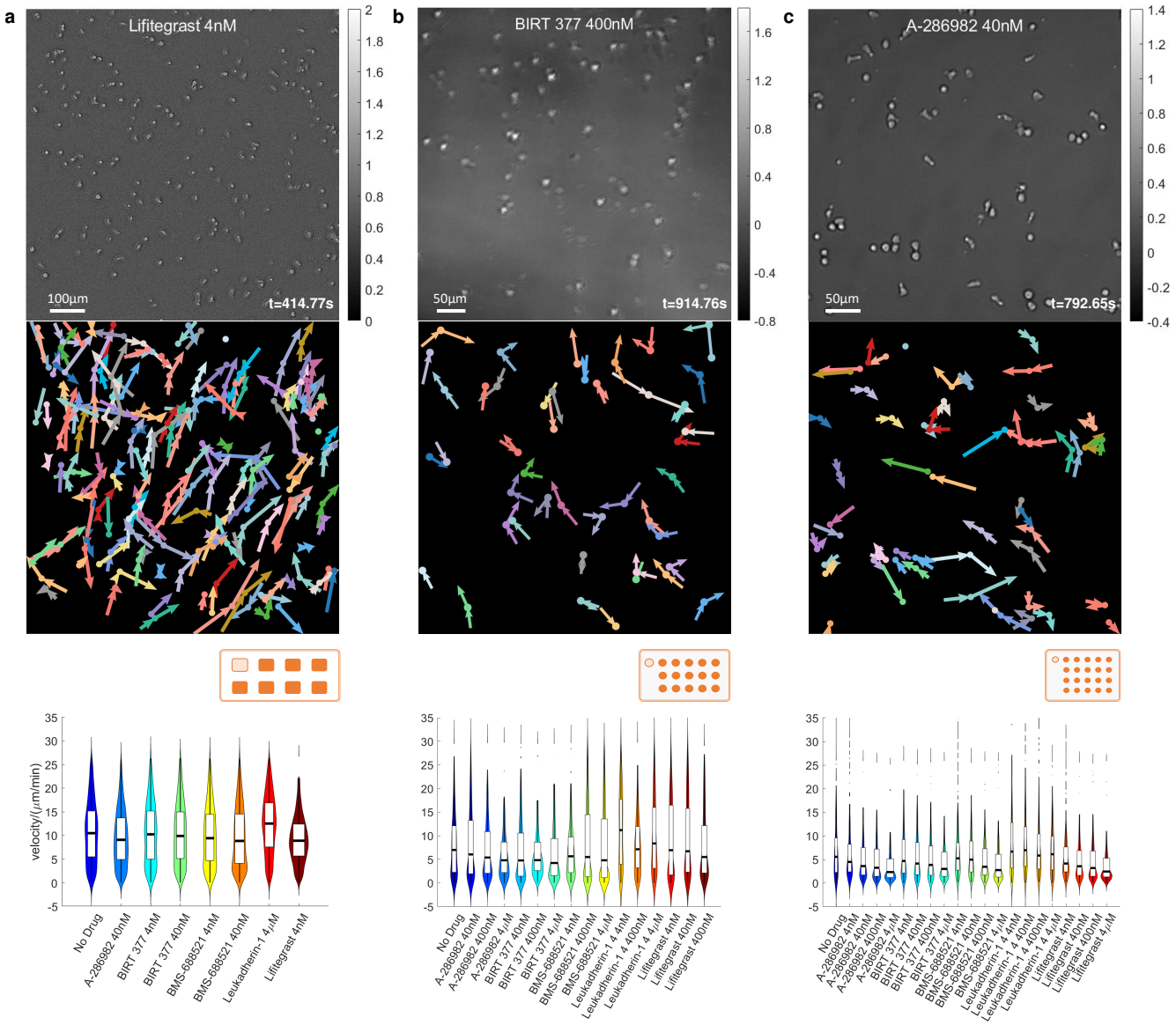


Figure 4. Miniaturized drug screening QPI performed with multiple experimental setups and five compounds including A-286982, BIRT 377, BMS-688521, Leukadherin-1, and Lifitegrast. (a) (Upper) The representative QPI result at 414.77s performed with an eight-well chambered coverglass plate, 10× objective lens, and 4nM Lifitegrast. (Middle) The velocity vector diagram corresponding to the representative phase image. (Lower) The violin plot of cell migration velocity derived from the eight-well experiment. (b) The QPI result at 914.76s performed with a 48-well cell culture plate, 20× objective lens, and 400nM BIRT 377, followed by the corresponding velocity vector diagram and the violin plot. (c) The QPI result at 792.65s performed with a 384-well cell culture plate, 25× objective lens, and 40nM A-286982, followed by the corresponding velocity vector diagram and the violin plot.

replace the bottom material of the Petri dish with matching glass, and have found available and cost-efficient solutions for manufacturing the containers. As a representative example, the QPI performed with the customized container and a $40\times 1.25 N.A.$ water immersion objective is demonstrated in Supplementary Fig. 7. In addition, when using an upright microscope in observing non-cellular samples, it is also feasible to use the same strategy to place the customized component above the sample or just replace the cover glass. Supplementary Fig. 8 shows the QPI results of unstained mouse liver sections acquired with a $40\times$ objective lens. The reconstructed phase is further fed into the cycleGAN-based virtual histological staining workflow[86], where the design of cycle consistency loss ensures that the network quantitatively establishes the association between QPI results and H&E stained images, demonstrating the potential of our proposed method to assist clinical diagnosis in the future[87,88].

We are also pushing forward the landing and application of the proposed technology. Firstly, we are trying to build general accessories that can be mounted to commercial microscopes, providing a readily available imaging mode. Secondly, extending the proposed approach to lensless microscopes is another topic holding great potential for high-throughput on-chip analysis. We believe the proposed method will broadly benefit biological and pathological studies on live specimens and inspire new connections between different microscopic observation modalities.

Methods

Mathematics for spectral encoding of phase information. Theoretically, the maximal incident angle θ can be obtained from the nominal numerical aperture ($N.A.$) of the objective lens as $\theta = \arcsin\frac{N.A.}{n}$, with n being the refractive index of the medium between the objective and the cover glass (e.g., for a water dipping objective lens n=1.33). Further, we denote the thickness of the dispersive element as d, and its refractive indices at wavelengths λ_1 and λ_2 as n_1 and n_2 respectively, the distance between two recorded axial planes corresponding to two wavelengths can be calculated as

$$\Delta z = \frac{d\left(\tan\beta_1 - \tan\beta_2\right)}{\tan\theta}, \tag{1}$$

where

$$\beta_j = \arcsin\frac{\sin\theta}{n_j}, \quad j = 1,2. \tag{2}$$

After simple derivation, we can get

$$\Delta z = d\cos\theta\left(\frac{1}{\sqrt{n_1^2-\sin^2\theta}} - \frac{1}{\sqrt{n_2^2-\sin^2\theta}}\right). \tag{3}$$

The fabrication and specifications of the customized flat optical element. By referring to the required defocus distance of existing TIE-based phase retrieval algorithms, the spectral profile of the coating on the dispersive element and its thickness are optimized for fabrication. The wavelengths of the two narrow bands of the coating are designed to have similar transmittance through live cells, be well separated, and produce distinct cell contours. To this end, we select two central wavelengths, 490 and 690nm, from 12 single narrow band filters meeting the above conditions, with the customized spectral profiles shown in Fig. 1(d). The thickness of the dispersive glass is a tradeoff between phase characterization capability and compatibility. A thicker substrate is more sturdy and brings more distinguished features of images under the two wavebands, but cannot fit in the small working distance in high magnification observations. On the contrary, a thinner design has higher compatibility which is especially important in high-magnification microscopy but imposes challenges in fabrication. Thanks to the significant difference between the focusing positions of two selected wavelengths, a 0.5mm-thick dispersive substrate can be sufficient for most commonly used microscope settings.

Labeling for supervised learning. we employ a phase-deriving algorithm based on the Transport of Intensity Equation[50], i.e.,

$$\frac{\partial I(r)}{\partial z} = \nabla[I(r)\nabla\varphi(r)] \tag{4}$$

to provide ground truth for supervised learning, with I being the intensity image, r and z indices spatial and axial positions. By obtaining the axial gradient of intensity from a stack of defocused images[53], the above partial differential equation can be solved using various methods[65], among which we use DCT-TIE algorithm[79] due to its high efficiency and accuracy.

The design mechanism of the network. Since phase retrieval requires transforming the encoded measurement towards a counterpart with the same resolution but quite different appearances, it is not straightforward to apply existing image restoration algorithms for this task. Here we adapt from the Residual Channel Attention Network (RCAN)[80] and the Holistic Attention Network (HAN)[89], and design the architecture composed of 10 residual groups with each group consisting of 20 residual channel attention blocks, as shown in Supplementary Fig.1, based on the following considerations:

i Since the transformation is a resolution-keeping process and the phase is of dissimilar distribution to the input, we do not introduce up-sampling or down-sampling layers and generate a structure with constant width.

ii A convolutional layer is applied to the encoded measurement to avoid influence from the high-frequency fringes or sensor noise.

iii The "Residual In Residual" architecture is used for coarse-to-fine residual learning, where multiple residual groups and a long skip connection serve as the outer layer of residual learning structure. Each residual group contains multiple residual channel attention blocks and a short skip connection, achieving residual learning in the inner layer.

iv Each residual channel attention block first contains a rectified linear unit (ReLU) layer sandwiched between two convolutional layers, to increase the network depth and enhance the receptive fields. The output of the second convolutional layer is further fed into the channel attention mechanism, which is designed to adjust the weight of channels to focus the learning attention on more important or information-intensive channels. Compared to common convolutional neural networks which handle all feature maps with a fair paradigm, the attention-based approach emphasizes specific features, thus facilitating the reconstruction of low-frequency components in phase images.

v The outputs of residual groups are concatenated and input into a layer attention module, which further draws attention to the multi-level features from the shallow outputs to the deep ones, and the attention indicator is derived by weighting the correlation coefficients between the features. Due to the potential GPU memory overflow of the large channel 3D convolution and the fact that the phase features are generally not as rich as natural images, we have removed the channel-spatial attention module from the original HAN.

The architecture of the network. The implementation of the adopted network is based on the structure of coarse residual learning, with the whole architecture illustrated in Supplementary Fig. 1 which includes 10 residual groups shown in the yellow box and extracts a 64-channel deep feature map. By introducing the idea of fine residual learning, each designed residual group includes 20 residual channel attention blocks as shown in the blue box. The channel attention mechanism works by pooling each feature channel as a single point, which serves as the distinguished weight of each channel, highlighting the key components in phase reconstruction. Additionally, a layer attention module is introduced as shown in the green box. The module calculates the correlation matrix among the multi-level feature maps output by residual groups, and the matrix is set as the weights for fusing the feature maps generated by all residual groups into the final feature map, which is then added to the shallow feature map through the long skip connection. Finally, the 64-channel result is processed through a convolutional layer to obtain the single-channel reconstructed image.

Network training and inference. The mean squared error loss and the default Adam optimizer are adopted in the training procedure, where the learning rate is initially 0.0001 and the decay rate is 0.6 per 80 epochs. Each image in the training dataset is randomly cropped into 128×128 pixel patches, and the batch size is set to 8. This framework is implemented with PyTorch and performed on a server equipped with GeForce GTX3090 graphic cards (NVIDIA) and a Core i7-8700K CPU @ 3.7GHz (Intel). The final model with the smallest validation loss is achieved after $\sim$800 iterations, and the training takes $\sim$100 hours. In testing, we take the live-cell video frame-by-frame as input and conduct phase retrieval in a patchwise manner, with the same patch size as in training. The phase inference of each patch takes around 150ms.

T cell culture. CD8 T cells were isolated from C57BL/6J mice by CD8a Microbeads (Miltenyi) according to the manufacturer's instructions. The cells were expanded in vitro by immobilized anti-CD3 and anti-CD28 antibodies (bioXcell) in complete RPMI medium (Invitrogen) supplemented with 10% FBS, 2 mM L-Glutamine, 50 IU/mL penicillin, 50 μg/mL streptomycin and 10 ng/mL recombinant IL-2 (Peprotech). In the indicated experiments, T cells were retrovirally transduced to express the green fluorescent protein.

Imaging of T cell behavior. Imaging plates were precoated with 7.5 μg/mL of recombinant murine ICAM-1 (Biolegend) in PBS at 37°C for 3 hours. In the indicated experiments, plates were additionally coated with 10 μg/mL of anti-CD3 (BioXCell) for the activation of T cells. During imaging experiments, T cells were resuspended in RPMI medium supplemented with 2 mM L-Glutamine, 50 IU/mL penicillin, and 50 μg/mL streptomycin.

Experiment details. For the experiments of long-term integrin-mediated T cell migration and activation, the ground-truth phases for training data were derived from the brightfield z-axis stacks of some fixed cells cultured in the same environment, including five defocused images at axial intervals of 2μm. For the drug screening experiment under $10\times$ magnification, the z-axis stacks contain eight defocused images at axial intervals of 2.5μm. For the $20\times$ and $25\times$ experiments, the stacks contain five defocused images at axial intervals of 2μm and 1μm, respectively. In all of the above experiments, the focal stacks range from above to below the focal plane.

Especially in the T cell activation experiment, a small number of cells are first injected and adhered to the bottom of the Petri dish to obtain the focal plane of imaging. Afterward, more cells are added to the dish, and meanwhile, a video-rate acquisition is performed with an exposure time of 80ms per frame, fully recording the sedimentation, adhesion, and deformation of the cells in the FOV.

Besides, the morphology of live cells might be significantly different from the fixed specimen serving as training data, so one should culture and fix cells in live conditions to reduce the adverse effect.

Cell labeling and tracking. The cell labeling used in the experiments is implemented by the pixel classification module in ilastik[83], where the signal-background classifier for the retrieved phase images is learned from the manual annotation of $\sim$50 images. Furthermore, if the cells distribute densely and clumping occurs, the pipeline for identifying primary objects with the global Otsu thresholding method in Cellprofiler[82] is applied for segmentation. A representative segmentation result is shown in the bottom block of Fig. 1(f) and the zoomed-in results are shown in Fig. 1(g) together with the detailed reconstructed phase.

By tracking the centroid of each independent cell in the video of phase image, the cell velocity and dynamic changes can be quantitatively analyzed to study the influence on cells of different experimental conditions. For each frame, we first

conduct cell segmentation and derive the centroid coordinate as well as the area of each cell. Then, we match the cells between adjacent frames by searching for the pair of cells being close and similar areas. From the matching result along the sequence, we can obtain continuous cell trajectories.

Mass calculation from the QPI reconstruction. The dry mass of each cell is calculated by summing over the product of the dry mass surface density and the pixel area (i.e., size of the sensor unit) across all the covered pixels, where the derivation of the dry mass surface density follows the equation from Popescu et al's work[2,5,81]:

$$\sigma(x,y) = \frac{\lambda}{2\pi\alpha}\phi(x,y), \tag{5}$$

Here λ=550nm is the average wavelength, and α=0.2mL/g is the refraction increment. As an example, the dry mass histogram derived from the phase map in the middle block of Fig. 1(f) is shown in Fig. 1(h).

References

1. Barer, R. Refractometry and interferometry of living cells. *J. Opt. Soc. Am.* **47**, 545–556 (1957).
2. Barer, R. Determination of dry mass, thickness, solid and water concentration in living cells. *Nature* **172**, 1097–1098 (1953).
3. Zangle, T. A. & Teitell, M. A. Live-cell mass profiling: an emerging approach in quantitative biophysics. *Nat. Methods* **11**, 1221–1228 (2014).
4. Kandel, M. E. *et al.* Phase imaging with computational specificity (PICS) for measuring dry mass changes in sub-cellular compartments. *Nat. Commun.* **11**, 6256 (2020).
5. Park, Y., Depeursinge, C. & Popescu, G. Quantitative phase imaging in biomedicine. *Nat. Photonics* **12**, 578–589 (2018).
6. Zernike, F. Das phasenkontrastverfahren bei der mikroskopischen beobachtung. *Z. technische Physik* **16**, 454–457 (1935).
7. Zernike, F. How I discovered phase contrast. *Science* **121**, 345–349 (1955).
8. Nomarski, G. Nouveau dispositif pour l'observation en contraste de phase differentiel. In *Journal de Physique et le Radium*, vol. 16, S88–S88 (1955).
9. Popescu, G. *Quantitative phase imaging of cells and tissues* (McGraw-Hill Education, 2011).
10. Cotte, Y. *et al.* Marker-free phase nanoscopy. *Nat. Photonics* **7**, 113–117 (2013).
11. Chen, X., Kandel, M. E., Hu, C., Lee, Y. J. & Popescu, G. Wolf phase tomography (WPT) of transparent structures using partially coherent illumination. *Light. Sci. & Appl.* **9**, 142 (2020).
12. Zhang, D. *et al.* Bond-selective transient phase imaging via sensing of the infrared photothermal effect. *Light. Sci. & Appl.* **8**, 116 (2019).
13. Descloux, A. *et al.* Combined multi-plane phase retrieval and super-resolution optical fluctuation imaging for 4D cell microscopy. *Nat. Photonics* **12**, 165–172 (2018).
14. Cross, S. E., Jin, Y.-S., Rao, J. & Gimzewski, J. K. Nanomechanical analysis of cells from cancer patients. *Nat. Nanotechnol.* **2**, 780–783 (2007).
15. Wu, P.-H. *et al.* A comparison of methods to assess cell mechanical properties. *Nat. Methods* **15**, 491–498 (2018).
16. Cooper, K. L. *et al.* Multiple phases of chondrocyte enlargement underlie differences in skeletal proportions. *Nature* **495**, 375–378 (2013).
17. Kim, T. *et al.* White-light diffraction tomography of unlabelled live cells. *Nat. Photonics* **8**, 256–263 (2014).
18. Taute, K., Gude, S., Tans, S. & Shimizu, T. High-throughput 3D tracking of bacteria on a standard phase contrast microscope. *Nat. Commun.* **6**, 1–9 (2015).
19. Wen, H. *et al.* Subnanoradian X-ray phase-contrast imaging using a far-field interferometer of nanometric phase gratings. *Nat. Commun.* **4**, 2659 (2013).
20. Rivenson, Y., Zhang, Y., Günaydın, H., Teng, D. & Ozcan, A. Phase recovery and holographic image reconstruction using deep learning in neural networks. *Light. Sci. & Appl.* **7**, 17141–17141 (2018).
21. Rivenson, Y. *et al.* PhaseStain: the digital staining of label-free quantitative phase microscopy images using deep learning. *Light. Sci. & Appl.* **8**, 23 (2019).
22. Reed, J. *et al.* Rapid, massively parallel single-cell drug response measurements via live cell interferometry. *Biophys. J.* **101**, 1025–1031 (2011).
23. Streibl, N. Phase imaging by the transport equation of intensity. *Opt. Commun.* **49**, 6–10 (1984).
24. Tian, L. & Waller, L. Quantitative differential phase contrast imaging in an LED array microscope. *Opt. Express* **23**, 11394–11403 (2015).
25. Xiong, B. *et al.* Snapshot partially coherent diffraction tomography. *Phys. Rev. Appl.* **15**, 044048 (2021).
26. Nguyen, T. L. *et al.* Quantitative phase imaging: recent advances and expanding potential in biomedicine. *ACS Nano* **16**, 11516–11544 (2022).
27. Smith, F. Two half-shade devices for optical polarizing instruments. *Nature* **173**, 362–363 (1954).
28. Weart, S. R. & Cohen, I. B. Selected papers of great American physicists: The bicentennial commemorative volume of the American physical society 1976. *Am. J. Phys.* **45**, 883–884 (1977).
29. De Groot, P. J. Vibration in phase-shifting interferometry. *J. Opt. Soc. Am. A* **12**, 354–365 (1995).

30. Caspersson, T., Carlson, L. & Svensson, G. A scanning interference microscope arrangement. *Exp. Cell Res.* **7**, 601–602 (1954).

31. Knox, C. Holographic microscopy as a technique for recording dynamic microscopic subjects. *Science* **153**, 989–990 (1966).

32. Cuche, E., Bevilacqua, F. & Depeursinge, C. Digital holography for quantitative phase-contrast imaging. *Opt. Lett.* **24**, 291–293 (1999).

33. Milgram, J. H. & Li, W. Computational reconstruction of images from holograms. *Appl. Opt.* **41**, 853–864 (2002).

34. Mann, C. J., Yu, L., Lo, C.-M. & Kim, M. K. High-resolution quantitative phase-contrast microscopy by digital holography. *Opt. Express* **13**, 8693–8698 (2005).

35. Merola, F. *et al.* Tomographic flow cytometry by digital holography. *Light. Sci. & Appl.* **6**, e16241–e16241 (2017).

36. Gabor, D. A new microscopic principle. *Nature* **161**, 777–778 (1948).

37. Wang, Z. *et al.* Spatial light interference microscopy (SLIM). *Opt. Express* **19**, 1016–1026 (2011).

38. Yoneda, N., Onishi, A., Saita, Y., Komuro, K. & Nomura, T. Single-shot higher-order transport-of-intensity quantitative phase imaging based on computer-generated holography. *Opt. Express* **29**, 4783–4801 (2021).

39. Kim, K., Kim, K. S., Park, H., Ye, J. C. & Park, Y. Real-time visualization of 3-D dynamic microscopic objects using optical diffraction tomography. *Opt. Express* **21**, 32269–32278 (2013).

40. Awatsuji, Y., Sasada, M. & Kubota, T. Parallel quasi-phase-shifting digital holography. *Appl. Phys. Lett.* **85**, 1069–1071 (2004).

41. Witte, S. *et al.* Short-coherence off-axis holographic phase microscopy of live cell dynamics. *Biomed. Opt. Express* **3**, 2184–2189 (2012).

42. Baek, Y. & Park, Y. Intensity-based holographic imaging via space-domain Kramers–Kronig relations. *Nat. Photonics* **15**, 354–360 (2021).

43. Meier, R. W. Twin-image elimination in holography using single-sideband waves. *J. Opt. Soc. Am.* **59**, 358–359 (1969).

44. Sánchez-Ortiga, E., Doblas, A., Saavedra, G., Martínez-Corral, M. & Garcia-Sucerquia, J. Off-axis digital holographic microscopy: practical design parameters for operating at diffraction limit. *Appl. Opt.* **53**, 2058–2066 (2014).

45. Tian, L., Petruccelli, J. C. & Barbastathis, G. Nonlinear diffusion regularization for transport of intensity phase imaging. *Opt. Lett.* **37**, 4131–4133 (2012).

46. Kachar, B. Asymmetric illumination contrast: a method of image formation for video light microscopy. *Science* **227**, 766–768 (1985).

47. Choi, W. *et al.* Tomographic phase microscopy. *Nat. Methods* **4**, 717–719 (2007).

48. Kim, K. *et al.* Diffraction optical tomography using a quantitative phase imaging unit. *Opt. Lett.* **39**, 6935–6938 (2014).

49. Ling, R., Tahir, W., Lin, H.-Y., Lee, H. & Tian, L. High-throughput intensity diffraction tomography with a computational microscope. *Biomed. Opt. Express* **9**, 2130–2141 (2018).

50. Teague, M. R. Deterministic phase retrieval: a Green's function solution. *J. Opt. Soc. Am.* **73**, 1434–1441 (1983).

51. Teague, M. R. Image formation in terms of the transport equation. *J. Opt. Soc. Am. A* **2**, 2019–2026 (1985).

52. Zuo, C. *et al.* High-resolution transport-of-intensity quantitative phase microscopy with annular illumination. *Sci. Reports* **7**, 1–22 (2017).

53. Waller, L., Kou, S. S., Sheppard, C. J. & Barbastathis, G. Phase from chromatic aberrations. *Opt. Express* **18**, 22817–22825 (2010).

54. Chowdhury, S. *et al.* High-resolution 3D refractive index microscopy of multiple-scattering samples from intensity images. *Optica* **6**, 1211–1219 (2019).

55. Chen, M., Ren, D., Liu, H.-Y., Chowdhury, S. & Waller, L. Multi-layer Born multiple-scattering model for 3D phase microscopy. *Optica* **7**, 394–403 (2020).

56. Ledwig, P. & Robles, F. E. Epi-mode tomographic quantitative phase imaging in thick scattering samples. *Biomed. Opt. Express* **10**, 3605–3621 (2019).

57. Zheng, G., Horstmeyer, R. & Yang, C. Wide-field, high-resolution Fourier ptychographic microscopy. *Nat. Photonics* **7**, 739–745 (2013).

58. Zheng, G., Shen, C., Jiang, S., Song, P. & Yang, C. Concept, implementations and applications of Fourier ptychography. *Nat. Rev. Phys.* **3**, 207–223 (2021).

59. Wu, J., Lin, X., Liu, Y., Suo, J. & Dai, Q. Coded aperture pair for quantitative phase imaging. *Opt. Lett.* **39**, 5776–5779 (2014).

60. Chen, C. *et al.* PhaseRMiC: phase real-time microscope camera for live cell imaging. *Biomed. Opt. Express* **12**, 5261–5271 (2021).

61. Phillips, Z. F., Chen, M. & Waller, L. Single-shot quantitative phase microscopy with color-multiplexed differential phase contrast (cDPC). *PLoS ONE* **12**, e0171228 (2017).

62. Tian, L. & Waller, L. 3D intensity and phase imaging from light field measurements in an LED array microscope. *Optica* **2**, 104–111 (2015).

63. Zuo, C., Chen, Q., Qu, W. & Asundi, A. Noninterferometric single-shot quantitative phase microscopy. *Opt. Lett.* **38**, 3538–3541 (2013).

64. Picazo-Bueno, J. A. & Micó, V. Optical module for single-shot quantitative phase imaging based on the transport of intensity equation with field of view multiplexing. *Opt. Express* **29**, 39904–39919 (2021).

65. Yu, W. *et al.* Real time quantitative phase microscopy based on single-shot transport of intensity equation (ssTIE) method. *Appl. Phys. Lett.* **109**, 071112 (2016).

66. Schwiegerling, J. History of the Shack Hartmann wavefront sensor and its impact in ophthalmic optics. In *Fifty Years of Optical Sciences at The University of Arizona*, vol. 9186, 291–298 (SPIE, 2014).

67. Akondi, V. & Dubra, A. Accounting for focal shift in the Shack–Hartmann wavefront sensor. *Opt. Lett.* **44**, 4151–4154 (2019).

68. Freischlad, K. R. & Koliopoulos, C. L. Modal estimation of a wave front from difference measurements using the discrete Fourier transform. *J. Opt. Soc. Am. A* **3**, 1852–1861 (1986).

69. Huang, D. *et al.* High-speed live-cell interferometry: a new method for quantifying tumor drug resistance and heterogeneity. *Anal. Chem.* **90**, 3299–3306 (2018).

70. Bryngdahl, O. & Lohmann, A. Single-sideband holography. *J. Opt. Soc. Am.* **58**, 620–624 (1968).

71. Booth, M. J. Adaptive optical microscopy: the ongoing quest for a perfect image. *Light. Sci. & Appl.* **3**, e165–e165 (2014).

72. Pavani, S. R. P., Libertun, A. R., King, S. V. & Cogswell, C. J. Quantitative structured-illumination phase microscopy. *Appl. Opt.* **47**, 15–24 (2008).

73. Zhang, M. *et al.* Snapshot quantitative phase microscopy with a printed film. *Opt. Express* **26**, 24763–24774 (2018).

74. Kwon, H., Arbabi, E., Kamali, S. M., Faraji-Dana, M. & Faraon, A. Single-shot quantitative phase gradient microscopy using a system of multifunctional metasurfaces. *Nat. Photonics* **14**, 109–114 (2020).

75. Li, L. *et al.* Single-shot deterministic complex amplitude imaging with a single-layer metalens. *Sci. Adv.* **10**, eadl0501 (2024).

76. Wang, F. *et al.* Phase imaging with an untrained neural network. *Light. Sci. & Appl.* **9**, 1–7 (2020).

77. Bostan, E., Heckel, R., Chen, M., Kellman, M. & Waller, L. Deep phase decoder: self-calibrating phase microscopy with an untrained deep neural network. *Optica* **7**, 559–562 (2020).

78. Deng, M., Li, S., Goy, A., Kang, I. & Barbastathis, G. Learning to synthesize: robust phase retrieval at low photon counts. *Light. Sci. & Appl.* **9**, 36 (2020).

79. Zuo, C., Chen, Q. & Asundi, A. Boundary-artifact-free phase retrieval with the transport of intensity equation: fast solution with use of discrete cosine transform. *Opt. Express* **22**, 9220–9244 (2014).

80. Zhang, Y. *et al.* Image super-resolution using very deep residual channel attention networks. In *European Conference on Computer Vision*, 286–301 (2018).

81. Popescu, G. *et al.* Optical imaging of cell mass and growth dynamics. *Am. J. Physiol. Physiol.* **295**, C538–C544 (2008).

82. Carpenter, A. E. *et al.* Cellprofiler: Image analysis software for identifying and quantifying cell phenotypes. *Genome Biol.* **7**, 1–11 (2006).

83. Berg, S. *et al.* ilastik: Interactive machine learning for (bio) image analysis. *Nat. Methods* **16**, 1226–1232 (2019).

84. Krummel, M. F., Bartumeus, F. & Gérard, A. T cell migration, search strategies and mechanisms. *Nat. Rev. Immunol.* **16**, 193–201 (2016).

85. Dustin, M. L. T-cell activation through immunological synapses and kinapses. *Immunol. Rev.* **221**, 77–89 (2008).

86. Zhu, J.-Y., Park, T., Isola, P. & Efros, A. A. Unpaired image-to-image translation using cycle-consistent adversarial networks. In *Proceedings of the IEEE International Conference on Computer Vision*, 2223–2232 (2017).

87. Martell, M. T. *et al.* Deep learning-enabled realistic virtual histology with ultraviolet photoacoustic remote sensing microscopy. *Nat. Commun.* **14**, 5967 (2023).

88. Jo, Y. *et al.* Label-free multiplexed microtomography of endogenous subcellular dynamics using generalizable deep learning. *Nat. Cell Biol.* **23**, 1329–1337 (2021).

89. Niu, B. *et al.* Single image super-resolution via a holistic attention network. In *European Conference on Computer Vision*, 191–207 (Springer, 2020).

Supplementary information

There are one Supplementary Document with eight figures and three supplementary videos.

Acknowledgements

This work is jointly funded by the Beijing Natural Science Foundation (Grant No. Z200021) and the National Natural Science Foundation of China (Grant Nos. 61931012, 62088102).

Author contributions

J. S. and W. Z. conceived this project. X. L., J. S., and W. Z. designed the experiments, X. L., W. Z. and W. M. conducted the experiments, W. Z. and J. S. analyzed the results. Q. D. and H. Q. supervised this research. All the authors participated in the writing of this paper.

Competing interests

The authors declare that there is no conflict of interest.

Supplementary Files

This is a list of supplementary files associated with this preprint. Click to download.

- SupplDoc.pdf
- Tcellmigration.avi
- Tcellactivation.avi
- drugscreening.avi